Science Robotics

robotics.sciencemag.org/cgi/content/full/2/10/eaao4369/DC1

Supplementary Materials for

Robotic metamorphosis by origami exoskeletons

Shuhei Miyashita,* Steven Guitron, Shuguang Li, Daniela Rus*

*Corresponding author. Email: shuhei.miyashita@york.ac.uk (S.M.); rus@csail.mit.edu (D.R.)

Published 27 September 2017, *Sci. Robot.* **2**, eaao4369 (2017)
DOI: 10.1126/scirobotics.aao4369

The PDF file includes:

Other Supplementary Material for this manuscript includes the following:
(available at robotics.sciencemag.org/cgi/content/full/2/10/eaao4369/DC1)

Materials and Methods

Remote Magnetic Control

The following sections derive the control of the coils by currents to obtain targeted magnetic torque and force for controlling the robot. The four coils (numbered $i \in 1, ..., 4$) are placed in counter-clockwise order seen from above at regular intervals around the central vertical axis in the lower hemisphere of diameter $d\,(= 65.2\,\text{cm})$ of the stage. This configuration provides the upper half hemisphere with an open space for robot operation. Each coil is inclined 45° from the horizontal plane such that the axes of symmetry intersect at the center of the sphere (set as the origin, ${}^{G}O$, of global coordinate ${}^{G}\hat{X}\hat{Y}\hat{Z}$, where the ${}^{G}\hat{X}$-$\hat{Y}$ plane is set horizontal, see Fig. S1).

The local coordinate frame of coil i, ${}^{i}\hat{x}\hat{y}\hat{z}$ is defined for each coil, where the origins of the local coordinate frames are located at the centroids of the coils ${}^{i}o$. The ${}^{i}\hat{x}$-$\hat{y}$ plane is parallel to the diametrical plane of the coil, and ${}^{i}\hat{z}$ is normal to the plane, coinciding with other ${}^{j}\hat{z}$ ($j \in 1, ..., 4; j \neq i$) axes of the coils at ${}^{G}O$.

The magnetic flux density produced by coil i along the central axis at position z relative to

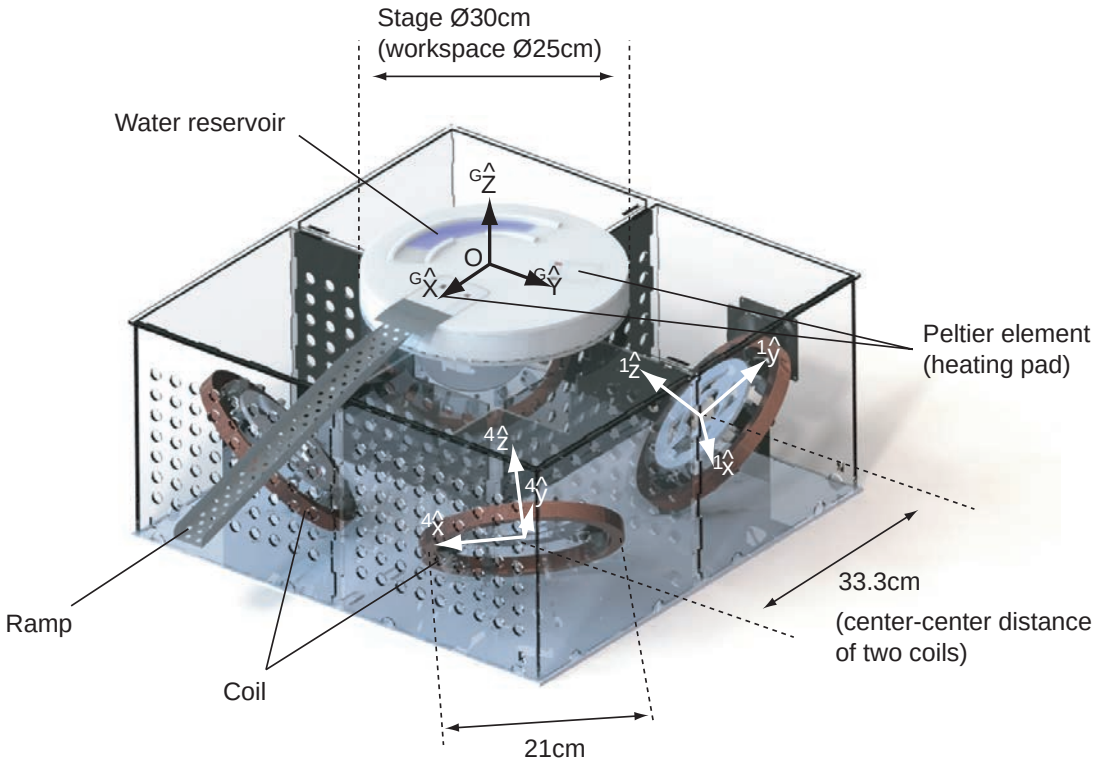

Figure S1. The platform. Coordinates are added from Fig. 5.

a coordinate frame ${}^i\hat{x}\hat{y}\hat{z}$ is

$$ {}^i\vec{b}_i = \begin{pmatrix} {}^ib_i(x) \\ {}^ib_i(y) \\ {}^ib_i(z) \end{pmatrix} = \frac{\mu_0 N a^2}{2(a^2 + {}^iz^2)^{\frac{3}{2}}} \begin{pmatrix} 0 \\ 0 \\ I_i \end{pmatrix}, \tag{1} $$

where $\vec{I} = (I_1,\, I_2,\, I_3,\, I_4)^T$ is the current vector consisting of traversing current of coil i, I_i, μ_0 ($= 4\pi \cdot 10^{-7}$ H/m) is the vacuum permeability, a ($= 21$ cm) is the diameter of coil, and N ($= 125$ turns) is the number of turns of wire of each coil. Due to the symmetry, $\vec{b}_x = \vec{b}_y = 0$.

The rotation matrix R_i for coil i to coincide the directions of axes of local frames ${}^i\hat{x}\hat{y}\hat{z}$ with those of global frame ${}^G\hat{X}\hat{Y}\hat{Z}$ can be expressed with Euler angles as

$$ R_i = R({}^i\hat{x}, -\frac{\pi}{4}) R({}^i\hat{z}', \phi_i), \tag{2} $$

where

$$R({}^{i}\hat{x},\theta) = \begin{bmatrix} 1 & 0 & 0 \\ 0 & \cos\theta & -\sin\theta \\ 0 & \sin\theta & \cos\theta \end{bmatrix} \tag{3}$$

and

$$R({}^{i}\hat{z}',\phi) = \begin{bmatrix} \cos\phi & -\sin\phi & 0 \\ \sin\phi & \cos\phi & 0 \\ 0 & 0 & 1 \end{bmatrix}. \tag{4}$$

Here $\phi_i = -\frac{\pi}{4}, -\frac{3\pi}{4}, \frac{3\pi}{4}$, and $\frac{\pi}{4}$ for coils $i = 1, ..., 4$, respectively, and ${}^{i}\hat{z}'$ is newly created axis by the first rotation about $\hat{x}$.

${}^{i}\vec{b}_i$ in the global coordinate ${}^{G}\vec{b}_i$ can be therefore obtained as

$${}^{G}\vec{b}_i = R^{-1}({}^{i}\hat{z}',\phi)\, R^{-1}({}^{i}\hat{x}, -\frac{\pi}{4})\, {}^{i}\vec{b}_i. \tag{5}$$

The globally created magnetic flux density by four coils ${}^{G}\vec{B}$ is given by the superposition of the individual magnetic flux densities ${}^{G}\vec{b}_i$ produced by respective coils, represented in the global coordinate, ${}^{G}\vec{b}_i$, as

$$\begin{aligned} {}^{G}\vec{B} &= \sum_{i=1}^{4} {}^{G}\vec{b}_i && (6)\\ &= \sum_{i=1}^{4} R^{-1}({}^{i}\hat{z}',\phi)\, R^{-1}({}^{i}\hat{x}, -\frac{\pi}{4})\, {}^{i}\vec{b}_i && (7)\\ &:= J(\hat{X},\hat{Y},\hat{Z})\, \vec{I}, && (8) \end{aligned}$$

where

$$J(\hat{X},\hat{Y},\hat{Z}) = \frac{\mu_0 N a^2}{2(a^2 + \frac{d^2}{4})^{\frac{3}{2}}} \begin{bmatrix} \frac{1}{2} & \frac{1}{2} & -\frac{1}{2} & -\frac{1}{2} \\ -\frac{1}{2} & \frac{1}{2} & \frac{1}{2} & -\frac{1}{2} \\ \frac{1}{\sqrt{2}} & \frac{1}{\sqrt{2}} & \frac{1}{\sqrt{2}} & \frac{1}{\sqrt{2}} \end{bmatrix}, \tag{9}$$

relating current $\vec{I}$ to magnetic flux density ${}^{G}\vec{B}$. (9) shows that (6) is linear in the current $\vec{I}$.

As J is full-rank, ${}^{G}\vec{B}$ produced at the center of the stage can be along any spherical direction and be of arbitrary strength up to the system's capacity. Our model can produce maximum magnetic flux density of $1.75\,\mathrm{mT}$ with current $48\,\mathrm{A}$, though this value can be varied by regulating the current flow or the number of wire turns in each coil.

One solution for the current $\vec{I}$ required to generate a desired magnetic flux density ${}^{G}\vec{B}$ at the stage can be determined by solving the unconstrained least squares problem

$$\underset{\vec{I}}{\text{minimize}} \; \| J(\hat{X}, \hat{Y}, \hat{Z})\, \vec{I} - {}^{G}\vec{B}(\hat{X}, \hat{Y}, \hat{Z}) \|_2 \tag{10}$$

corresponding to the undetermined system of (8). The least squares problem (10) can be solved using the Moore-Penrose pseudo inverse of the matrix J

$$\vec{I} = J^{\#}\, {}^{G}\vec{B}, \tag{11}$$

where $J^{\#} = J^T (J J^T)^{-1}$. This minimizes the Euclidean norm of $\vec{I}$, thereby minimizing both energy consumption and heat generation (*39*).

We obtain

$$J^{\#} = \frac{2(a^2 + \frac{d^2}{4})^{\frac{3}{2}}}{\mu_0 N a^2} \begin{bmatrix} \frac{1}{2} & -\frac{1}{2} & \frac{1}{2\sqrt{2}} \\ \frac{1}{2} & \frac{1}{2} & \frac{1}{2\sqrt{2}} \\ -\frac{1}{2} & \frac{1}{2} & \frac{1}{2\sqrt{2}} \\ -\frac{1}{2} & -\frac{1}{2} & \frac{1}{2\sqrt{2}} \end{bmatrix}. \tag{12}$$

The attachment mechanisms require precise localization, which can be provided via magnetic sensing, vision, or an external tracking and localization system. While localization using magnetic sensing was demonstrated on our platform in (*44*), due to the complexity of the environment and necessity for multimodal performance, a human operator manually controlled alignment and direction.

In practice, as ${}^{G}\vec{b}_i$ diverges, the system experiences deviations in the direction and strength of ${}^{G}\vec{B}$ at around the edge of the workspace. To warrant the controllability of robots, the system was designed with four coils instead of the minimum number, three, to reasonably cancel out the deviations of the field strengths by oppositely positioning coils (close one and distant one). Additionally, the diameter of the coils was set such that their normal projections onto the stage cover the entire area and minimizes the deviation in the direction of produced magnetic field.

Primer **Control**

Primer has an edge length of $3.18\,\mathrm{mm}$, weighs $0.24\,\mathrm{g}$, with a surface field of $0.65\,\mathrm{T}$ (***K&J magnetics***). By regarding the magnet as a magnetic dipole $\vec{m} := (m(X),\, m(Y),\, m(Z))^T$, the magnetic torque $\vec{\tau}$ acting on the magnet due to ${}^G\vec{B}$ is given by

$$\vec{\tau} = \vec{m} \times {}^G\vec{B} \tag{13}$$

$$= \begin{bmatrix} 0 & -m(Z) & m(Y) \\ m(Z) & 0 & -m(X) \\ -m(Y) & m(X) & 0 \end{bmatrix} {}^G\vec{B}. \tag{14}$$

We experimentally estimated $m = 0.030\,\mathrm{Am}^2$ by measuring required torque to rotate *Primer*. With (8) and (14) follows that $\vec{\tau}$ is linear in the currents $\vec{I}$. Therefore,

$$\vec{\tau} := J_\tau\, \vec{I}, \tag{15}$$

where

$$J_\tau = \frac{\mu_0 N a^2}{2(a^2 + \frac{d^2}{4})^{\frac{3}{2}}} \cdot \begin{bmatrix} -\frac{1}{2}m(Z) - \frac{1}{\sqrt{2}}m(Y) & \frac{1}{2}m(Z) - \frac{1}{\sqrt{2}}m(Y) \\ \frac{1}{2}m(Z) - \frac{1}{\sqrt{2}}m(Y) & -\frac{1}{2}m(Z) - \frac{1}{\sqrt{2}}m(Y) \\ -\frac{1}{2}m(Z) + \frac{1}{\sqrt{2}}m(X) & -\frac{1}{2}m(Z) + \frac{1}{\sqrt{2}}m(X) \\ \frac{1}{2}m(Z) + \frac{1}{\sqrt{2}}m(X) & \frac{1}{2}m(Z) + \frac{1}{\sqrt{2}}m(X) \\ \frac{1}{2}m(Y) + \frac{1}{2}m(X) & \frac{1}{2}m(Y) - \frac{1}{2}m(X) \\ -\frac{1}{2}m(Y) - \frac{1}{2}m(X) & -\frac{1}{2}m(Y) + \frac{1}{2}m(X) \end{bmatrix} \tag{16}$$

which relates current $\vec{I}$ to torque $\vec{\tau}$. We estimate $\tau_{\max} = 5.25 \cdot 10^{-5}\,\mathrm{Nm}$ ($0.535\,\mathrm{g\text{-}f\,cm}$) under the application of ${}^G B = 1.75\,\mathrm{mT}$, which assures the possible-to-lift surface area of $1.21\,\mathrm{cm}^2$ assuming that the sheet is flat square, the density of second exoskeleton sheet $0.0344\,\mathrm{g/cm}^2$, and the magnet positions at the center of the sheet. Based on the calculation, the developed exoskeletons have off-centered *Primer* positions close to the pivoting point to reduce the required torque, with comprehensive body structures to enable larger exoskeleton sizes.

Walk-bot

The *Walk-bot* design is shown in Fig. S2. The unfolded exoskeleton has size $23.72 \times 8.09\,\mathrm{mm}^2$. When folding, the creases consisting of 13 mountain folds and 17 valley folds self-fold, encasing

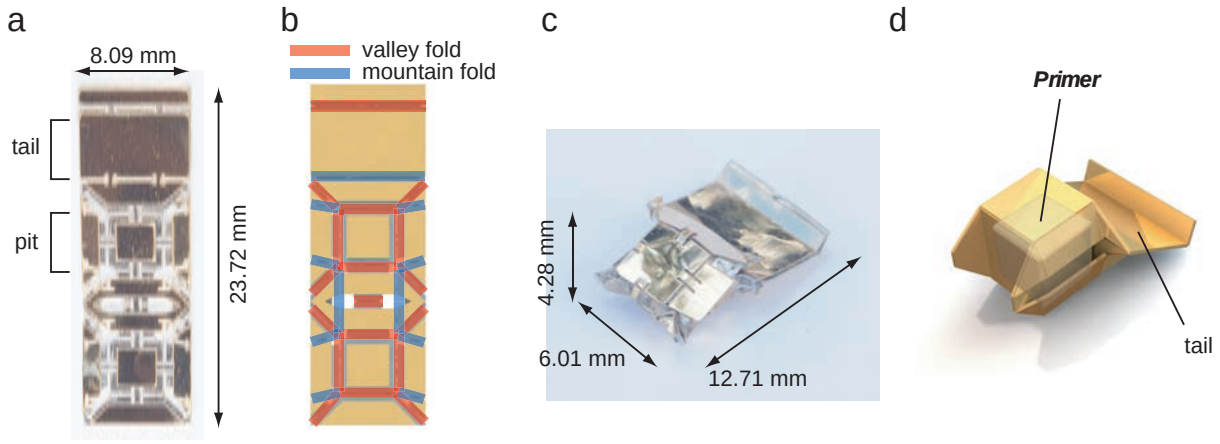

Figure S2. Walk-bot design. (a,b) unfolded configurations, and (c,d) folded configurations.

Primer completely. The average time taken for self-folding of *Walk-bot* is $173\,\mathrm{s}$ (5 samples). The speed typically depends on the capacity of the Peltier element and can be increased by using another type or soaking in hot water (*46*). Once self-folded, *Walk-bot* stands at $4.25\,\mathrm{mm}$ tall and is $10.43 \times 7.81\,\mathrm{mm}^2$. It weighs $0.289\,\mathrm{g}$ while merely 17% of the weight is from the exoskeleton (the rest is from *Primer*). The walking motion is based on stick-slip motion presented also in (*29*).

Scaled walk-bot

The design of *Scaled walk-bot* is shown in Fig. S3. It weighs $0.539\,\mathrm{g}$; *Walk-bot* including *Primer* weighs $0.289\,\mathrm{g}$, which is 53.6% of the total weight. The basic crease pattern was inherited from *Walk-bot* but without the front segment that reconfigures to a ceiling. Instead, four arms are provided at the location of *Walk-bot*, facing the short edge. A self-folding process turns the unfolded sheet of $32.82 \times 22.14\,\mathrm{mm}^2$ into *Scaled walk-bot* ($26.9 \times 21.94 \times 6.11\,\mathrm{mm}^3$). The

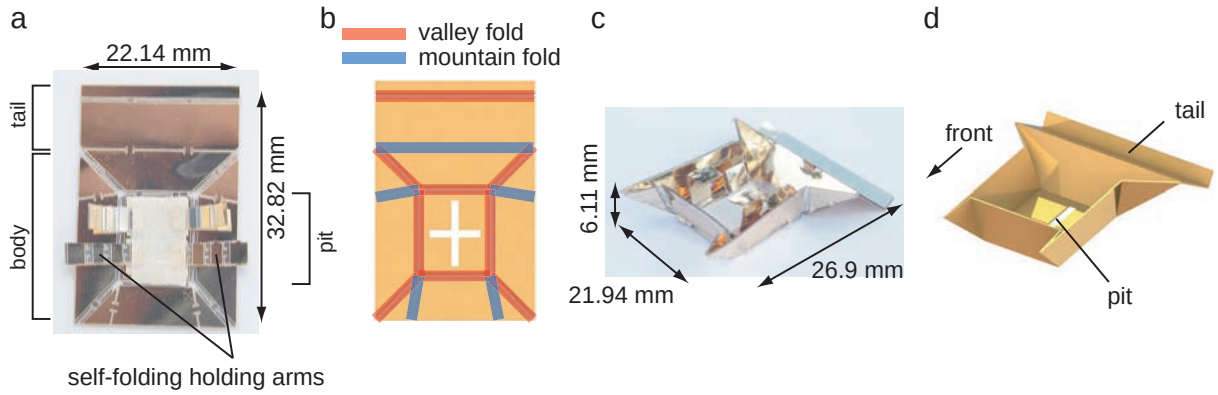

Figure S3. Scaled walk-bot design. (a,b) unfolded configurations, and (c,d) folded configurations.

process involves 5 mountain folds and 9 valley folds. The average self-folding speed of a second exoskeleton is 158 s (5 samples). The body size was chosen according to the maximum amount of magnetic torque we can impose. The tail was shortened to reduce the amount of torque required to pivot.

The *Scaled walk-bot* is particularly useful as a miniature shovel. To demonstrate its effectiveness, we measured the carriable number of $\sim$ 5 mm polyethylene foam blocks of 2 mg for *Scaled walk-bot* and *Walk-bot*. While *Walk-bot* was able to carry at most one block at a time, *Scaled walk-bot* could carry between 3 and 5 blocks at one time.

The experiment of 2-step metamorphoses and molting processes shown in Fig. 2 (a)-(f) was iterated for 5 times and we obtained 2 end-to-end successes. The time taken for the whole process was around 20 min in average (3 samples). The variable time was spent aligning *Walk-bot* to the exoskeleton and waiting for the latches to dissolve. The main reason for the failure is misalignment of *Walk-bot* in the exoskeleton of *Scaled walk-bot*. While *Walk-bot* can walk under water, the capillary force prevents it from coming ashore. In experiments, we employed rolling motion for *Walk-bot* when it climbed the slope. The success and failure of events occurring in each trial are detailed in Table 1.

Table S1. Success and failure events with Scaled walk-bot.

	Primer alignment	*Walk-bot* self-folding	*Walk-bot* walking	*Walk-bot* alignment	*Scaled walk-bot* self-folding	*Scaled walk-bot* walking	*Scaled walk-bot* dissolving	*Walk-bot* molting
Trial 1	Yes	Yes	Yes	No	No	No	No	No
Trial 2	Yes	Yes	Yes	Yes	Yes	No	Yes	Yes
Trial 3	Yes	Yes	No	No	No	No	No	No
Trial 4	Yes	Yes	Yes	Yes	Yes	Yes	Yes	Yes
Trial 5	Yes	Yes	Yes	Yess	Yes	Yes	Yes	Yes

Wheel-bot

The design of *Wheel-bot* is shown in Fig. S4. The unfolded exoskeleton of *Wheel-bot* has a

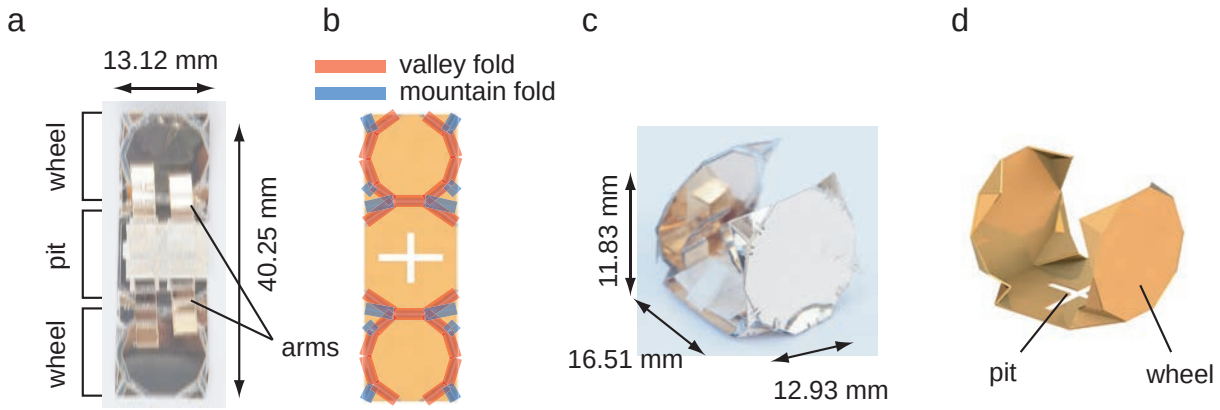

Figure S4. Wheel-bot design. (a,b) unfolded configurations, and (c,d) folded configurations.

dimension of $40.25 \times 13.12\,\mathrm{mm}^2$ and consists of three blocks. It weighs $0.43\,\mathrm{g}$, while *Walk-bot* including *Primer* weighs $0.298\,\mathrm{g}$. *Walk-bot* sits at the pit facing the longitudinal edge. When heated, 12 mountain and 20 valley folds self-fold, and two parts on both ends transform into decagonal wheels perpendicularly folding up. The angle of the wheel is regulated with a pair of mountain and valley folds, and the angle converges near perpendicularly to the pit. It achieves a dimension of $12.93 \times 16.51 \times 11.83\,\mathrm{mm}^3$. Ideally, the *Primer* should be positioned around the wheel axis. However, such design would require elevation of *Walk-bot* while self-folding, and *Walk-bot* could fall out of the latch. Once reconfiguration is completed, a rotational magnetic field of $1.75\,\mathrm{mT}$ is applied for rolling motion. In experiments, the frequency is set at $0.73\,\mathrm{Hz}$.

Fig. S5 shows the rolling speed of *Wheel-bot* over the frequency of rotational magnetic field. As expected, the speed linearly increases proportional to the frequency until step-out

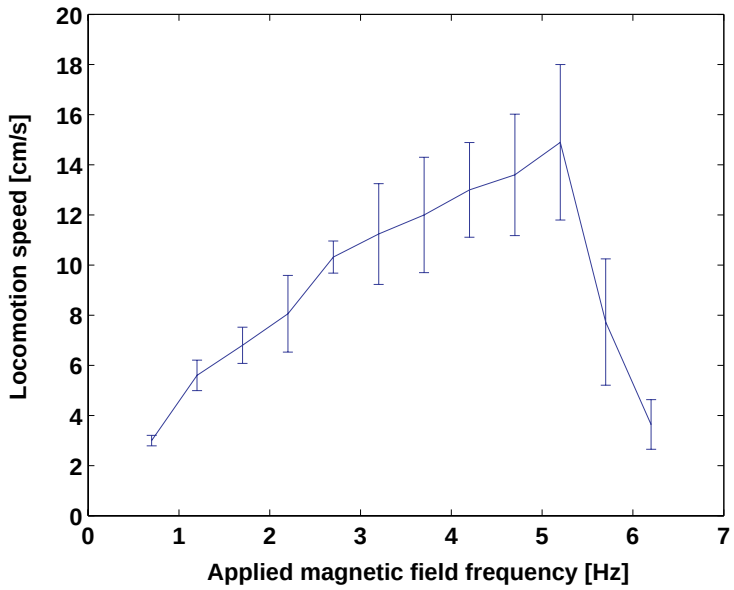

Figure S5. The rolling speed of Wheel-bot over frequency of magnetic field applied (five samples).

occurs after 5 Hz. *Wheel-bot* rolls at a maximum speed of 14.8 cm/s, while *Walk-bot* walks at a maximum speed of 5.84 cm/s, showing the efficiency of rolling on ground (270% faster).

The robot capability enabled by the wheel exoskeleton added to *Walk-bot* is shown in Fig. S6. Due to the simple crease pattern, the entire process shows reliable performance. The trial was repeated 5 times with 4 successes. The success and failure of events occurring in each trial are detailed in Table 2.

Boat-bot

Boat-bot shows stability when controlled on water and can move on ground using stick-slip motion due to the forward placement of the magnet. Fig. S7 shows the crease pattern (a,b) and the self-folded *Boat-bot* (c,d). The unfolded exoskeleton sheet (31.44×19.64 mm^2, 0.496 g)

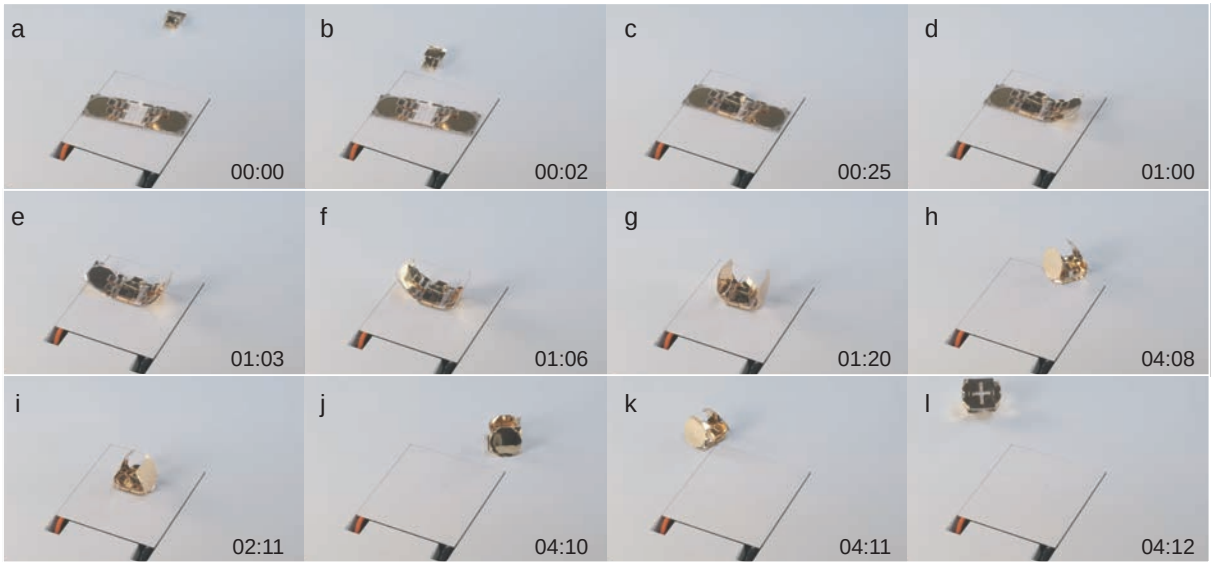

Figure S6. Demonstration of Wheel-bot. (a-c) *Walk-bot* approaches and steps on the wheel exoskeleton. (d-i) The exoskeleton starts heat-triggered self-folding, (j-l) forms two wheels on both sides, and starts rolling, guided by a magnetic field. The entire experiment is presented in Movie 2.

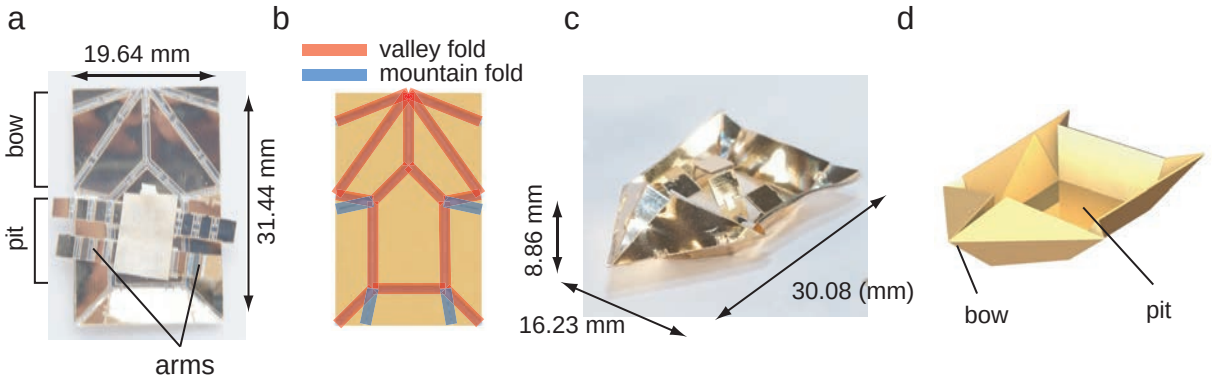

Figure S7. Boat-bot design. (a,b) unfolded configurations, and (c,d) folded configurations.

self-folds into a boat shape of $30.08 \times 16.23 \times 8.86\,\text{mm}^3$ by lifting the sides up, forming a concave shape around the pit. The process involves 4 mountain and 14 valley folds, which self-fold into a concave body shape for floating.

For actuation on water, we employ magnetic force induction with field gradient. Given no

Table S2. Success and failure events with Wheel-bot.

	Walk-bot alignment	*Wheel-bot* self-folding	*Wheel-bot* rolling	*Wheel-bot* dissolving	*Walk-bot* molting
Trial 1	Yes	Yes	Yes	Yes	Yes
Trial 2	Yes	Yes	Yes	Yes	Yes
Trial 3	Yes	Yes	Yes	Yes	Yes
Trial 4	Yes	Yes	Yes	Yes	Yes
Trial 5	Yes	Yes	No	Yes	Yes

current is running in the space occupied by *Primer*, the magnetic force F acting on *Primer* with magnetic moment $\vec{m}$ due to ${}^{G}\vec{B}$ is given by

$$\vec{F} = (\vec{m} \cdot \nabla)\, {}^{G}\vec{B} \tag{17}$$

$$= \begin{bmatrix} \frac{\partial\, {}^{G}\vec{B}(X)}{\partial X} & \frac{\partial\, {}^{G}\vec{B}(X)}{\partial Y} & \frac{\partial\, {}^{G}\vec{B}(X)}{\partial Z} \\ \frac{\partial\, {}^{G}\vec{B}(Y)}{\partial X} & \frac{\partial\, {}^{G}\vec{B}(Y)}{\partial Y} & \frac{\partial\, {}^{G}\vec{B}(Y)}{\partial Z} \\ \frac{\partial\, {}^{G}\vec{B}(Z)}{\partial X} & \frac{\partial\, {}^{G}\vec{B}(Z)}{\partial Y} & \frac{\partial\, {}^{G}\vec{B}(Z)}{\partial Z} \end{bmatrix} \begin{pmatrix} m(X) \\ m(Y) \\ m(Z) \end{pmatrix} \tag{18}$$

$$= \begin{pmatrix} \frac{\partial\, {}^{G}\vec{B}}{\partial X} m(X) \\ \frac{\partial\, {}^{G}\vec{B}}{\partial Y} m(Y) \\ \frac{\partial\, {}^{G}\vec{B}}{\partial Z} m(Z) \end{pmatrix}. \tag{19}$$

From (7), we obtain

$$\frac{\partial\, {}^{G}\vec{B}}{\partial X} = \sum_{i=1}^{4} \frac{\partial}{\partial X} \vec{b}_i \tag{20}$$

$$= \sum_{i=1}^{4} \frac{\partial}{\partial z_i} \frac{\partial z_i}{\partial X} \frac{\mu_0 N a^2 I_i}{2(a^2 + z_i^2)^{\frac{3}{2}}} \tag{21}$$

$$= \frac{3\mu_0 N a^2}{4} \left\{ -\sum_{i=1}^{2} \left(\frac{z_i^2 I_i}{(a^2 + z_i^2)^{\frac{5}{2}}} \right) + \sum_{i=3}^{4} \left(\frac{z_i^2 I_i}{(a^2 + z_i^2)^{\frac{5}{2}}} \right) \right\}. \tag{22}$$

By substituting $z_i = \frac{d}{2}$ for all i, we obtain

$$\frac{\partial\, {}^{G}B}{\partial X} = \frac{3}{4} \mu_0 N a^2 \left\{ \frac{\frac{d^2}{4}}{(a^2 + \frac{d^2}{4})^{\frac{5}{2}}} \right\} (-I_1 - I_2 + I_3 + I_4). \tag{23}$$

Similarly, we obtain

$$\frac{\partial\, {}^{G}B}{\partial Y} = \frac{3}{4} \mu_0 N a^2 \left\{ \frac{\frac{d^2}{4}}{(a^2 + \frac{d^2}{4})^{\frac{5}{2}}} \right\} (I_1 - I_2 - I_3 + I_4) \tag{24}$$

and

$$\frac{\partial\, {}^{G}B}{\partial Z} = \frac{3}{2\sqrt{2}}\mu_0 N a^2 \left\{ \frac{\frac{d^2}{4}}{(a^2+\frac{d^2}{4})^{\frac{5}{2}}} \right\} (-I_1 - I_2 - I_3 - I_4). \tag{25}$$

(17)-(25) suggest that $\vec{F}$ is linear in the current $\vec{I}$ and can be rewritten as

$$\vec{F} = J_F\, \vec{I}, \tag{26}$$

where

$$\begin{aligned} J_F =& \frac{3}{4}\mu_0 N a^2 \left\{ \frac{\frac{d^2}{4}}{(a^2+\frac{d^2}{4})^{\frac{5}{2}}} \right\} \cdot \\ & \begin{bmatrix} -m(X) & -m(X) & m(X) & m(X) \\ m(Y) & -m(Y) & -m(Y) & m(Y) \\ -\sqrt{2}m(Z) & -\sqrt{2}m(Z) & -\sqrt{2}m(Z) & -\sqrt{2}m(Z) \end{bmatrix}, \end{aligned} \tag{27}$$

which relates current $\vec{I}$ to force $\vec{F}$.

We use negative currents $I_i \leq 0$ and always use attractive force for swimming control regardless of the position of the *Primer* on the stage. With (23), we estimate magnetic force $F(X) = 0.0378\,\text{mN}$ under application of $I_1 = I_2 = -10\,\text{A}$ assuming that a magnet is pointing toward the positive direction of $\hat{X}$-axis.

With (15) and (26) follows

$$\begin{pmatrix} \vec{\tau} \\ \vec{F} \end{pmatrix} = \begin{bmatrix} J_\tau \\ J_F \end{bmatrix} \vec{I} := A\, \vec{I}, \tag{28}$$

where A is a 6×4 actuation matrix describing the torque and force acting on a magnet inside the area of operation due to the currents applied by the four electromagnetic coils. By solving the inverse of A, we obtain required $\vec{I}$ for desired $\vec{F}$ and $\vec{\tau}$. This linear transformation enables real-time production of magnetic field in response to the operator's control input.

The payload of *Boat-bot* was measured by placing increasing weight ($\varnothing 2.38\,\text{mm}$, $0.0204\,\text{g}$ aluminum balls) onto the exoskeleton. The result was $0.924 \pm 0.066\text{g}$ (5 samples) before it

sank. Given the weight of *Walk-bot* is 0.496 g, it carries 1.86 times its weight by equipping the boat exoskeleton.

The entire experiment with *Boat-bot*, starting with *Walk-bot* is shown in Fig. S8. The process

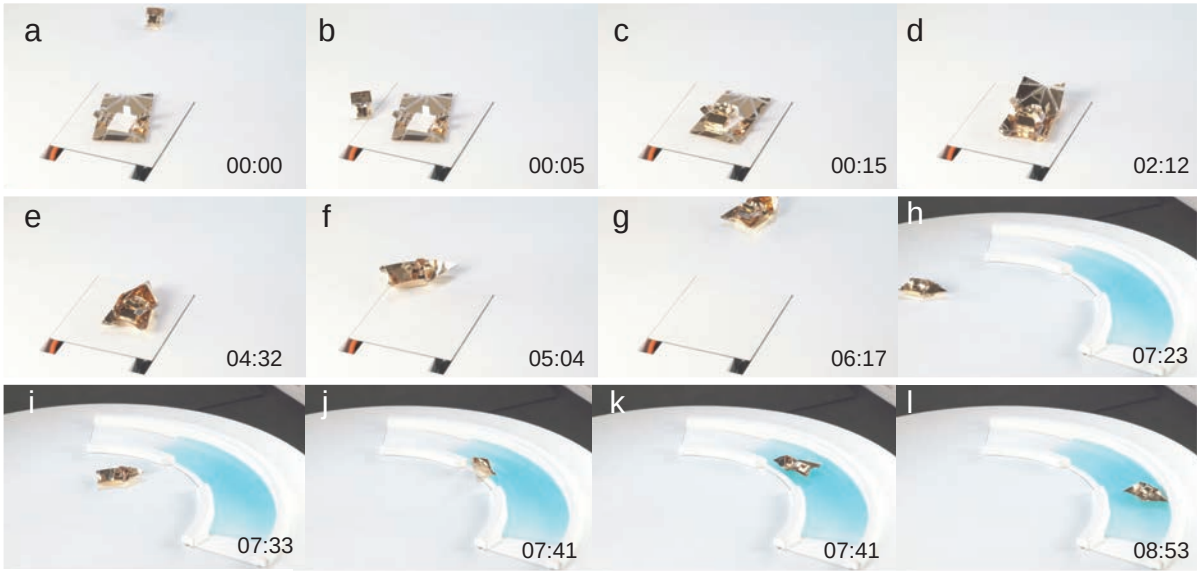

Figure S8. Demonstration with boat exoskeleton. The *Walk-bot* walks in and rides on the pit of the boat exoskeleton (a-c). The exoskeleton starts self-folding (d), and completes reconfiguration (e). The folded exoskeleton walks and enters the reservoir (f-i). It shows swimming capability on water (j-l). The entire experiment is presented in Movie 3.

was iterated 5 times and 3 successful results were obtained. We detailed the success and failure of events occurring in each trial in Table 3. In the two failure trials, *Boat-bot* failed to walk due to misalignment of *Walk-bot*.

Glider-bot

The exoskeleton of *Glider-bot* and the folded configurations are shown in Fig. S9. The design requires extensive considerations of weight and strength for the structure, and aerodynamics for the gliding motion. Additionally, there are design constraints from the size of Peltier element,

Table S3. Success and failure events with Boat-bot.

	Walk-bot alignment	*Boat-bot* self-folding	*Boat-bot* walking	*Boat-bot* floating
Trial 1	Yes	Yes	No	Yes
Trial 2	Yes	Yes	No	No
Trial 3	Yes	Yes	Yes	Yes
Trial 4	Yes	Yes	Yes	Yes
Trial 5	Yes	Yes	Yes	Yes

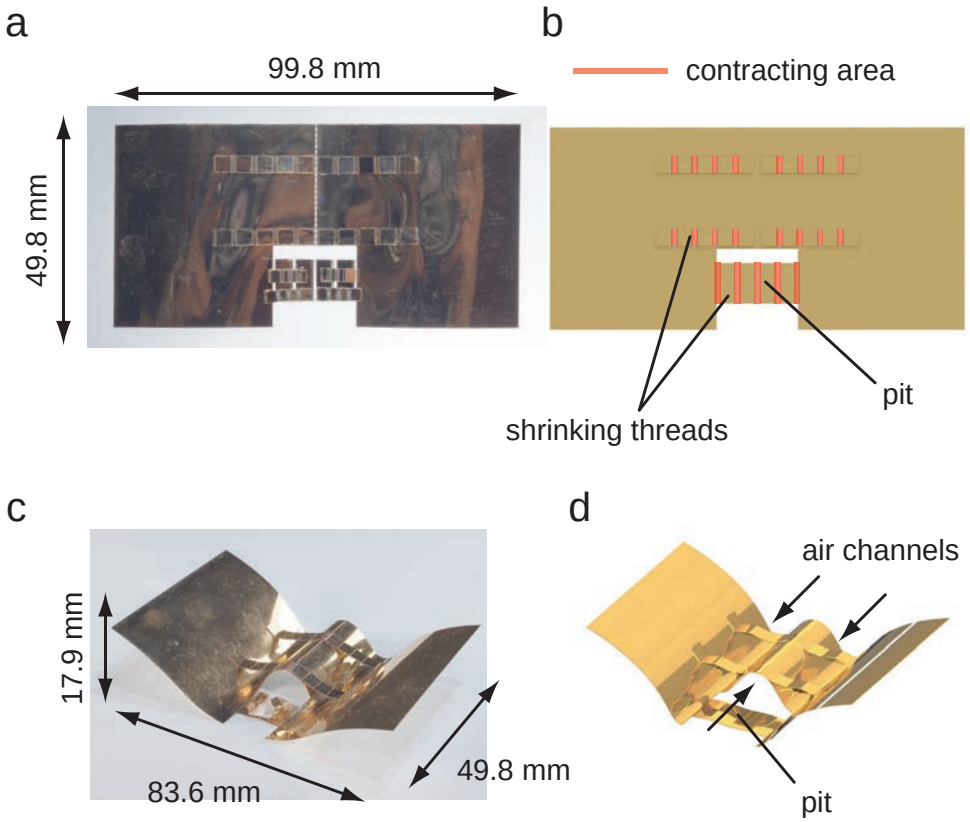

Figure S9. Glider-bot design. (a,b) unfolded configurations and (c,d) folded configurations.

that all the contracting threads should fit in the area. In order to increase the stability about the roll axis, the *Glider-bot* has a W-shaped body with three cylindrical opening channels. This design allows the wing on each side to be kept upward with a dihedral angle of approximately $33 \pm 2^{\circ}$ (6 samples). Moreover, these symmetrical channels act as stabilizers to keep the robot's

gliding posture without yaw motion. To form the wing shape, six linear heat-sensitive shrinking threads are attached. When heat is applied to the structure, the threads contract and produce the curved wing shape. This design lowers the center of mass and lifts up the wing, enabling a proper gliding posture with stability about the pitch axis. The structure can be made with a single layer and thus it is lightweight while maintaining enough rigidity against twisting and bending when gliding. In addition, the shape provides a space for the pit for *Walk-bot* to position itself. The sheet has a dimension $99.8 \times 49.8\,\text{mm}^2$ and once it configures as *Glider-bot* it has a dimension $83.6 \times 49.8 \times 17.9\,\text{mm}^3$. The body of *Glider-bot* exoskeleton weighs $0.585\,\text{g}$ and the body of *Glider-bot* including *Walk-bot* weighs $0.825\,\text{g}$.

We have demonstrated a successful end-to-end cycle for gliding. The success and failure of events occurring in each trial are detailed in Table 4. The main reasons for failure were

Table S4. Success and failure events with Glider-bot.

	Walk-bot alignment	*Glider-bot* self-folding	*Glider-bot* ramp sliding	*Glider-bot* gliding
Trial 1	Yes	Yes	Yes	Yes
Trial 2	Yes	Yes	No	No
Trial 3	Yes	Yes	Yes	No
Trial 4	Yes	Yes	Yes	No
Trial 5	Yes	No	No	No

misalignment of the walk bot on exoskeleton, misfolding of the *Glider-bot* exoskeleton (the wings would buckle or fold non-symetrically), and inability to fly once folded. The challenge has been alignment with the gliding ramp, due to the significantly larger size of *Glider-bot*. Producing a glider at this scale with self-folding methods has proven to be an exacting process where even a small misalignment of Walk-bot could spell the difference between success and failure. Our challenge was designing around the immense difficulties of flight at this scale, to which we have achieved a complete successful end-to-end cycle.

Multimedia Extension

We provide four movies that display the typical metamorphic behavior of (1) *Scaled walk-bot* as shown in Fig. 2 (Movie 1), (2) *Wheel-bot* as shown in Fig. S6 (Movie 2), (3) *Boat-bot* as shown in Fig. S8 (Movie 3), and (4) *Glider-bot* as shown in Fig. 2 (Movie 4).